Electronic Supplementary Information (ESI)
Thermal conductivity Measurements of Thin films by Non-Contact Scanning Thermal Microscopy Under Ambient Conditions

Yun Zhang, Wenkai Zhu, and Theodorian Borca-Tasciuc*
Mechanical, Aerospace, and Nuclear Engineering Department
Rensselaer Polytechnic Institute, Troy, NY 12180 USA

1. Supplemental equations for the analytical model of the active probe and probe parameters

For the probe region between $[0, L\text{-}b]$ and $[L\text{+}b, 2L]$ the heat transfer equation yields:

$$\frac{d^2T^*}{dx^2} - (\frac{2h_{\text{eff}}}{k_p r} - \frac{I^2\rho_0 TCR_p}{k_p \pi^2 r^4})T^* + \frac{I^2\rho_0}{k_p \pi^2 r^4} = 0 \tag{S1}$$

With the boundary condition for the edge of the probe:

$$T^*\big|_{x=0} = T^*\big|_{x=2L} = 0 \tag{S2}$$

and the boundary condition at the apex:

$$-k_p A_p \frac{\partial T^*}{\partial x}\Big|_{x=L-b} + \frac{I^2\rho_0 b}{A_p}(1 + TCR_p \times T^*\big|_{x=L-b}) - h_{\text{eff}} b\pi r T^*\big|_{x=L-b} = \frac{Q_s}{2} \tag{S3}$$

The coefficients C_3 and C_4 in Eqn. (14) of the article are shown as:

$$C_3 = \frac{\dfrac{q_0 b^2}{2k_p r_p^2} - \dfrac{\Gamma}{\lambda}e^{-\lambda(L-b)} - \Gamma b - (\Gamma b TCR_p - \dfrac{2hb}{k_p r_p})\dfrac{\Gamma}{\lambda^2}(1 + e^{-\lambda(L-b)})}{-\lambda\cosh(\lambda(L-b)) + (\Gamma b TCR_p - \dfrac{2hb}{k_p r_p})\sinh(\lambda(L-b))} \tag{S4}$$

$$C_4 = \frac{\Gamma}{\lambda^2} - C_3 \tag{S5}$$

Table S1. Wollaston probe parameters used by the 3DFEM and Analytical Model (AM). Parameters used by only one model specify the model in parenthesis

Attribute	Symbol	Unit	Value in model
Probe wire radius	R	µm	2.5
Probe half length	L	µm	100
Probe tip radius of curvature (3DFEM)	R_{curve}	µm	12
Half angle of probe's V shape (3DFEM)	Θ	degree	27
Thermal conductivity of probe	k_p	Wm^{-1}K^{-1}	38
Probe electrical resistivity (19.9 ºC)	ρ_0	Ω·m	2.06×10^{-7}
Applied current	I	mA	12.4
Temperature coefficient of resistance	TCR_p	K^{-1}	0.00165
Effective heat transfer coefficient (AM)	h	Wm^{-2}K^{-1}	1700

2. Thin film temperature profile comparisons between the analytical model and 3DFEM

The sample geometry used for validation consists of a thin film disk with a thickness of 240 nm, a radius of 100 μm and a substrate with the same radius and thickness of 1 mm. The same thermal conductivity for each domain is input into the analytical model and 3DFEM, where k_s=1.1 Wm^{-1}K^{-1}. The Gaussian heat flux profile from 3DFEM is fitted to yield a Gaussian radius and a peak heat flux and is then input into the analytical model. A comparison between the temperature profiles of the analytical and 3DFEM results for k_f = 240 Wm^{-1}K^{-1} and 340 Wm^{-1}K^{-1} is shown in Fig. S1. The temperature rises in the center and the edge are well-matched in the analytical model and in 3DFEM with different k_f, which leads to very similar thermal resistances in terms of Eqn. (13), with a discrepancy of less than 0.35%.
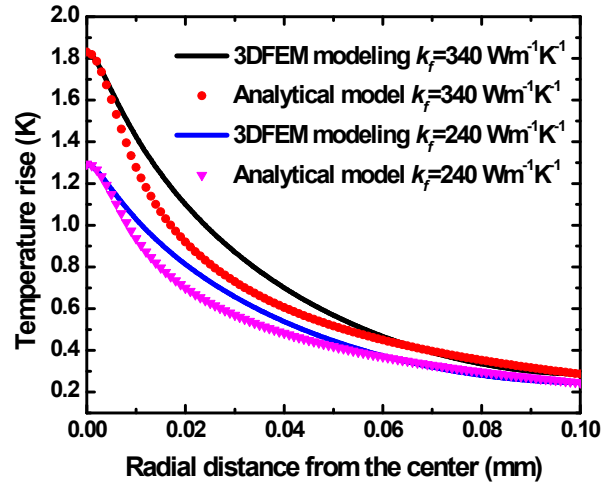
Fig. S1. Comparison of temperature rise above ambient between analytical and 3DFEM results

3. Gaussian radii comparison for different probe orientations

Figure S2 shows the similar Gaussian radii fitted for the heat flux in the sample plane along directions parallel and perpendicular to the probe plane. Results are shown for k_f = 240 Wm^{-1}K^{-1} on k_s = 1.1 Wm^{-1}K^{-1}.
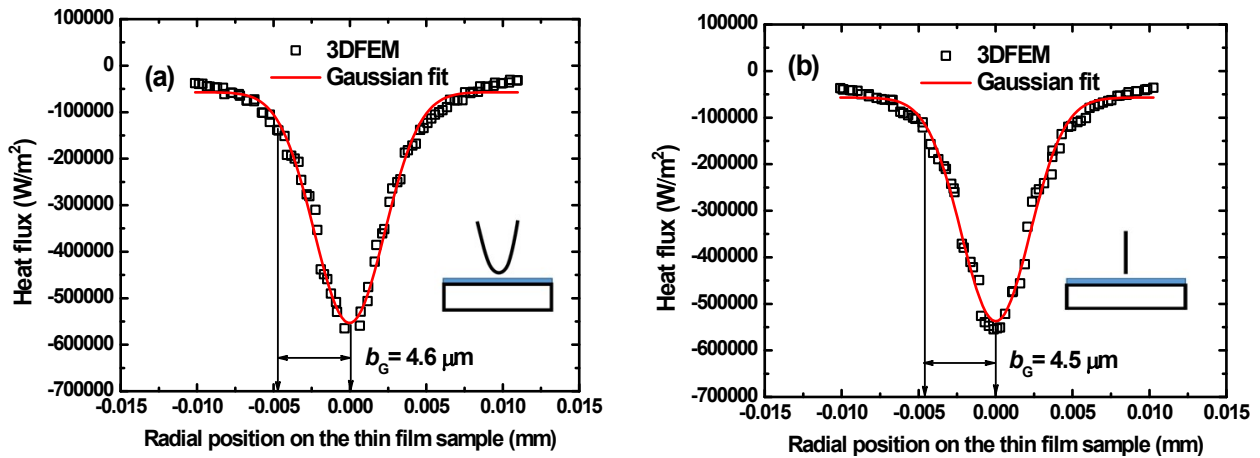
Fig. S2. Gaussian fitting of sample surface heat flux where the direction of the profile is: (a) parallel to the probe plane; (b) perpendicular to the probe plane. The probe plane is indicated by the V-shape of the probe.

4. Gaussian radii comparison for bulk and film-on-substrate samples with different thermal conductivity

The geometries of the bulk sample are 100μm radius and 1mm thickness and its k_b are set to 1.1Wm^{-1}K^{-1} and 50 Wm^{-1}K^{-1} respectively. The b_{GC} for each thermal conductivity case is obtained by taking the square root of the product of b_G along the two orientations (similar to the schematics shown in Fig. S2). Figure S3 shows b_{GC} is invariant at 5.4 μm ±0.1 μm for the range of k_b = 1.1~50 Wm^{-1}K^{-1}. Ref.[1] provided R_C^{th} vs. b curves of different k_b = 0.5~50 Wm^{-1}K^{-1} and all curves intersected at 5.35 μm ± 0.1 μm. Comparing b and b_{GC}, the similar value being observed demonstrates the assumption of equivalent b and b_{GC} for bulk samples is valid.
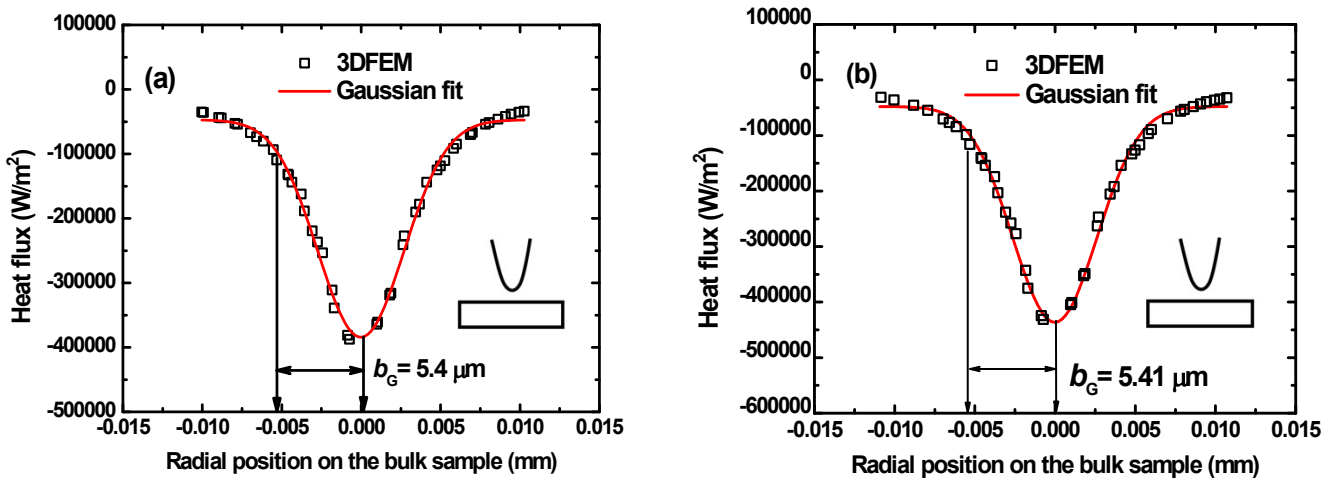
Fig. S3. Gaussian heat flux distribution of the bulk sample from 3DFEM with: (a) k_b = 1.1 Wm^{-1}K^{-1}; (b) k_b = 50 Wm^{-1}K^{-1}.

The values of b_G for k_f = 10 Wm^{-1}K^{-1} and 1000 Wm^{-1}K^{-1} with the substrate (k_s=1.1 Wm^{-1}K^{-1}) are obtained by 3DFEM. Figure S4 shows b_G for thin film-on-substrate samples is almost unchanged when k_f is changed from 10 to 1000 Wm^{-1}K^{-1}. Therefore, an initial value of $b = b_{GC}$ = 4.6 μm ± 0.1 μm was selected for the thin film-on-substrate sample. This value was fine-tuned as described in section 6 of the article.
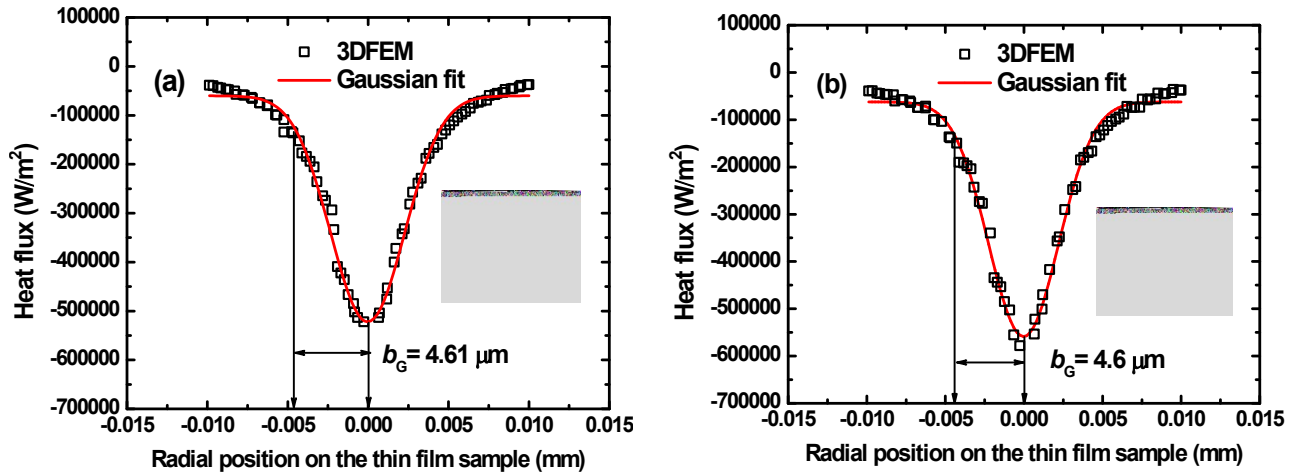
Fig. S4. Gaussian heat flux distribution of the thin film-on-glass sample from 3DFEM with: (a) k_f=10Wm^{-1}K^{-1}; (b) k_f = 1000 Wm^{-1}K^{-1}.

5. Gaussian radii comparison for different tip-sample clearances

The Gaussian heat flux distributions at apex tip-sample clearances in the range of 100-300 nm for 240 nm k_f =240 $Wm^{-1}K^{-1}$ film on substrate (k_s=1.1 $Wm^{-1}K^{-1}$) are plotted in Fig. S5. The fitted Gaussian radii are found to be independent of tip-sample clearance.
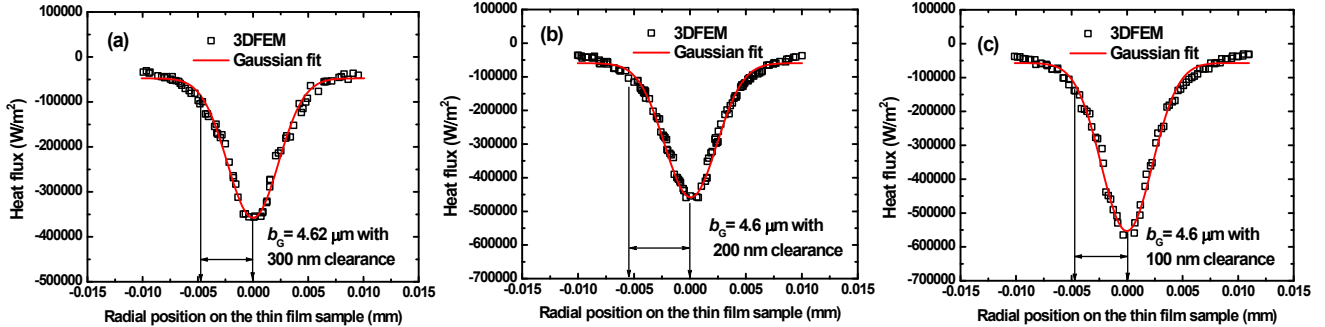
Fig. S5. Gaussian heat flux distribution of the thin film-on-substrate (glass) sample from 3DFEM with k_f = 240 $Wm^{-1}K^{-1}$ at tip-sample clearance of (a) 300 nm, (b) 200 nm, (c) 100 nm.

6. Silicon oxide film thermal conductivity measurement

Three SThM thermal resistance experiments were performed above the SiO_2 film on Si substrate and the probe thermal resistance at non-contact position (100nm tip-sample clearance) has a R_p^{th} of 23941±4.0 K/W. The thermal conductivity of the SiO_2 film obtained from the 3DFEM fitting is 1.19±0.08 $Wm^{-1}K^{-1}$ as shown in Fig. S6.
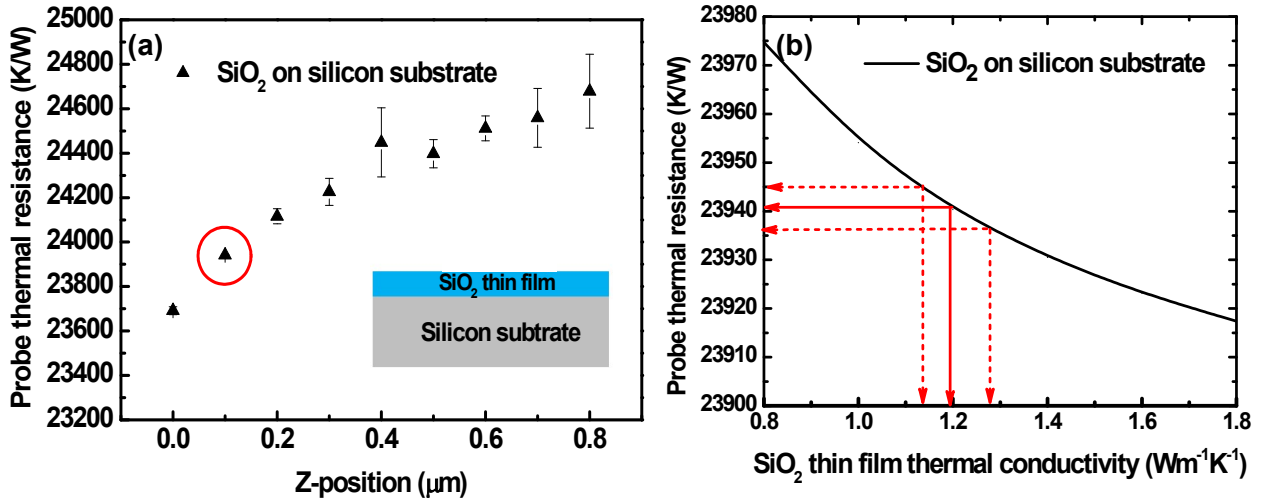
Fig. S6. (a) Probe thermal resistance vs. tip-sample clearance for silicon dioxide film on the silicon substrate measured at an apex tip-sample clearance of 100 ± 50 nm. The error bars are (max-min)/2 that are calculated based on three experiments; (b) 3DFEM predictions of R_p^{th} vs. thermal conductivity of the SiO_2 thin film on silicon substrate with 100 nm apex tip-sample clearance. Using the values of the experimental R_p^{th} the thermal conductivity and uncertainty of the SiO_2 thin film are determined by fitting, as shown by the red arrows.

7. Fitted functions of the product of t_f and k_f vs. R_p^{th} for films on glass and Si substrate samples

7.1 Film on glass substrate

Figure S7 compares the 3DFEM and analytical results from Fig. 10b) of the main article with Eq. (18) based numerical fitted functions using the parameters listed in Table III of the main article.
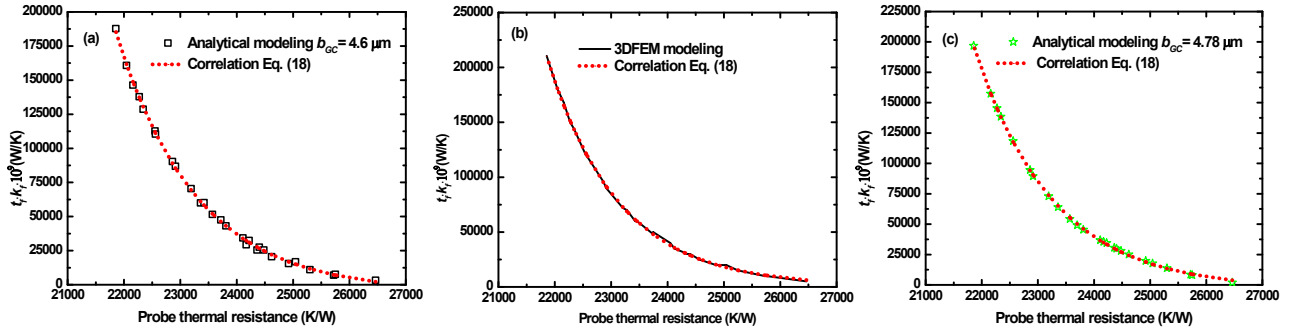
Fig. S7. Comparisons between t_f k_f based on Fig. 10b) values and the numerical fitted functions using the parameters listed in Table III of the article for: (a) analytical modeling with b_{GC} = 4.6 μm; (b) 3DFEM modeling; (c) analytical modeling with b_{GC} = 4.78 μm.

7.2 Film on Silicon substrate with interfacial SiO₂ layer

The fitted function for this case is developed based on the data from the 3-layer analytical model for the sample thermal resistance of a film on Si substrate with an SiO₂ interfacial layer and with b_{GC} = 4.78 μm. In the analytical model, the interfacial layer SiO₂ is set to the measured thermal conductivity of 1.19 Wm⁻¹K⁻¹ and thickness of 102 nm according to the thickness listed in Table I of the article. The analytical model predictions using the top film thickness and thermal conductivity range as t_f =46.6, 100, 240, 300 nm and k_f from 50 Wm⁻¹K⁻¹ to 600 Wm⁻¹K⁻¹ are fitted by Eq. (S6) with parameters shown in Table S2. The fit is shown in Fig. S8. The thermal conductivity of the Au film on Si substrate determined by this fitted function is 116.6 Wm⁻¹K⁻¹, which has a 16.7% discrepancy compared to k_f^{WF} shown in Table II of the main article.
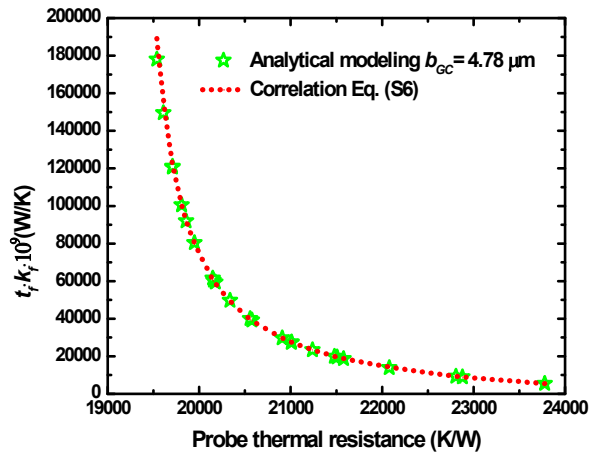
Fig. S8. Comparisons between the product t_f k_f based on the analytical modeling with b_{GC} = 4.78 μm and the fitting function Eq. (S6) with parameters from Table S2.

$$t_f \cdot k_f \cdot 10^9 = \frac{A_2}{\ln(R_p^{th} / A_1)} - A_0 \tag{S6}$$

Table S2. The fitted parameters and goodness of fit for Eqn. (S6) for thin films on silicon substrate with a 102nm SiO_2 interfacial film

	Analytical model
A1	19207.54
A2	3408.5495
A0	10536.80
R	0.99993

8. Photodetector signal for Au on glass and Si substrate samples

Figure S9 shows the photodetector voltage vs. probe-sample distance for the samples, as a representation of the cantilever deflection during SThM experiments. The point of contact is distinguished by an initial drop in the photodetector signal which is a result of the attracting forces at tip-sample close proximity, followed by a sudden rise due to the repulsion force at the contact.
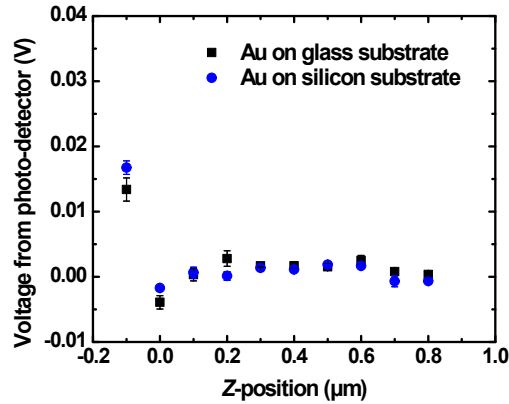
Fig. S9. The photodetector signals as a function of tip-sample clearance for Au on glass and Au on silicon substrate samples respectively. The voltage standard deviation is much smaller than the change produced by the tip-sample repulsion.

9. Estimation of the measured Au film thermal conductivity uncertainty due to height uncertainty in the transition regime

The numerical simulations shown in Fig 5 of the article predict an invariant probe thermal resistance in the 50nm-200nm height interval (23640 - 23641 K/W for Au on glass sample and 23777 - 23779 K/W for Au on silicon sample) which practically eliminates effects due to height uncertainty. For a conservative estimate of the experimental uncertainty of the fitted thermal conductivity due to the height uncertainty, the fitted functions (Eq. (18) and Eq. (S6)) developed for the 100nm tip-sample distance were used with the thermal resistances predicted at 50nm and 200nm (simulating hypothetical situations of large height uncertainties, when the tip-sample distances are actually 50nm or 200nm instead of the assumed 100nm). The fitted film thermal conductivities results are 216.2 - 216.4 $Wm^{-1}K^{-1}$ for the Au film on glass sample and 116.5 – 116.6 $Wm^{-1}K^{-1}$ for the Au film on silicon sample. The maximum uncertainty of film thermal conductivities due to height uncertainty is very small, less than 0.09%.

10. Ratio of the in-plane to cross-plane heat flux distributions as a function of depth in the films investigated in this work and for different in-plane radial distances from the probe apex
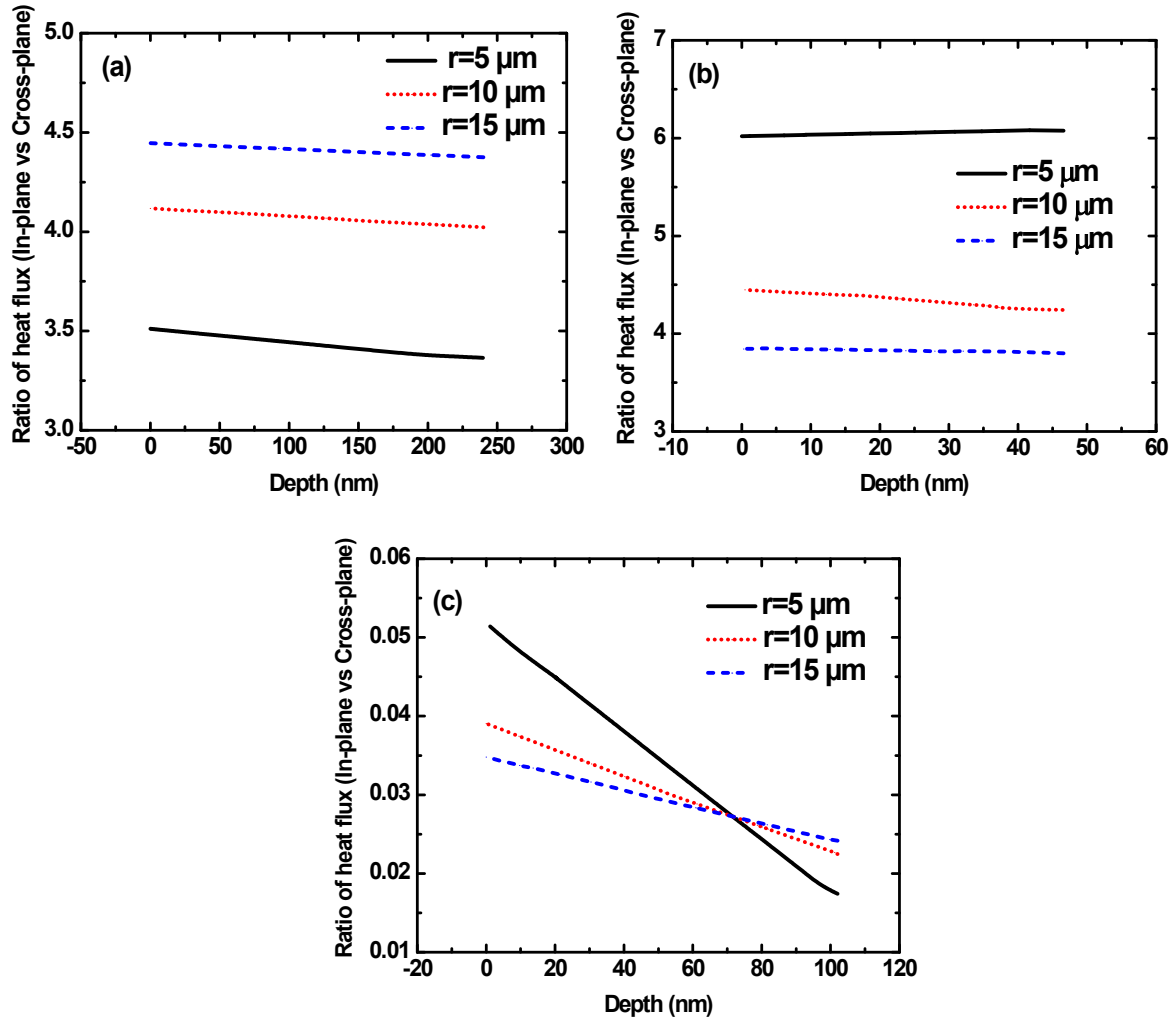
Fig. S10. Heat flux ratio (in-plane vs cross-plane) as a function of the depth below the film surface calculated at different radial distances r from the probe apex and for (a) Au film with $t_f = 240nm$, $k_f = 240$ $Wm^{-1}k^{-1}$ and with 1mm glass substrate; (b) Au film with $t_f = 46.6nm$, $k_f = 131$ $Wm^{-1}k^{-1}$ and with 102nm SiO_2 film and 1mm silicon substrate; (c) SiO_2 film with $t_f = 102nm$, $k_f = 1.19$ $Wm^{-1}k^{-1}$ and with 1mm silicon substrate.

Figure S10 shows the ratio of the in-plane to cross-plane heat flux for the three samples investigated in this work. As shown in S10 a) and b) the in-plane heat transfer is dominant in the Au films due to the spreading effect induced by a high k_f film on low k_s substrate/layer configuration. On another hand, as indicated by results shown in Fig. S10 c) the SiO_2 film on silicon has dominant heat transfer in the cross-plane direction due to the low k_f film on a high thermal conductivity substrate configuration.

11. Microscopy image and numerical temperature distribution of the experimental Wollaston wire probe

Figure S11a) shows an optical microscopy image of the probe used in this work. The probe used in the simulation has the dimensions and geometry based on the experimental probe, as summarized in Table S1. Figure S11b) shows the 3DFEM simulation of the temperature distribution of the Wollaston wire probe 100nm above the Au on glass substrate sample. Finer details of the temperature distribution in the sample are shown in Fig. S11c).
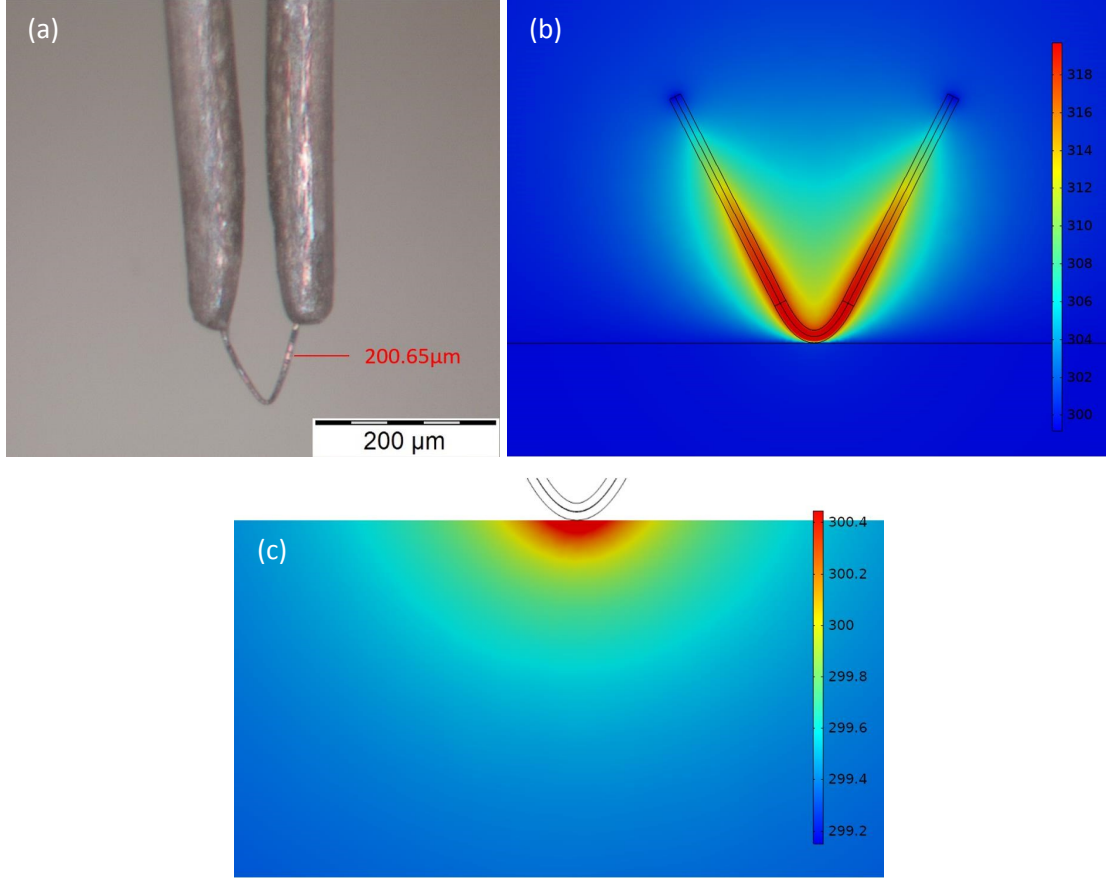
Fig. S11. (a) Optical microscopy image of the Wollaston wire probe; (b) Temperature distribution of the probe, the sample, and the ambient air when the probe is 100nm above the Au on glass substrate sample. (c) Finer details of the temperature profile in the sample near the tip apex.

12. Boundary conditions for the analytical model of the film-on-substrate sample

The boundary condition on top of the film:

$$-k_1 \frac{\partial T_1^*}{\partial z_1}\bigg|_{z_1=t_1} = q_0 e^{-r^2/b_{GC}^2} \tag{S7}$$

The boundary condition on sample bottom in case of a two-layer and a three-layer sample:

$$\left.\frac{\partial T_2^*}{\partial z_2}\right|_{z_2=0} = 0 \tag{S8}$$

$$\left.\frac{\partial T_3^*}{\partial z_3}\right|_{z_3=0} = 0 \tag{S9}$$

The boundary conditions for the radial direction (i=1:3, if 3 layers and i=1:2 if 2 layers):

$$\left.\frac{\partial T_i^*}{\partial r}\right|_{r=0} = 0 \tag{S10}$$

$$\left. T_i^* \right|_{r\to\infty} = 0 \tag{S11}$$

The boundary conditions across the interfaces (i=1:2 if 3 layers and i=1 if 2 layers):

$$\left. T_i^* \right|_{z_i=0} = \left. T_{i+1}^* \right|_{z_{i+1}=t_{i+1}} \tag{S12}$$

$$\left. k_i \frac{\partial T_i^*}{\partial z} \right|_{z_i=0} = \left. k_{i+1} \frac{\partial T_{i+1}^*}{\partial z} \right|_{z_{i+1}=t_{i+1}} \tag{S13}$$